

Tensor-reduced atomic density representations

James P. Darby*,¹ Dávid P. Kovács*,² Ilyes Batatia,^{2,3} Miguel A. Caro,⁴
Gus L. W. Hart,⁵ Christoph Ortner,⁶ and Gábor Csányi²

¹*Warwick Centre for Predictive Modelling, School of Engineering,
University of Warwick, Coventry, CV4 7AL, UK*

²*Engineering Laboratory, University of Cambridge, Cambridge, CB2 1PZ UK*

³*ENS Paris-Saclay, Université Paris-Saclay, 91190 Gif-sur-Yvette, France*

⁴*Department of Electrical Engineering and Automation, Aalto University, FIN-02150 Espoo, Finland*

⁵*Department of Physics and Astronomy, Brigham Young University, Provo, Utah, 84602, USA*

⁶*Department of Mathematics, University of British Columbia,
1984 Mathematics Road, Vancouver, BC, Canada V6T 1Z2*

(Dated: October 5, 2022)

Density based representations of atomic environments that are invariant under Euclidean symmetries have become a widely used tool in the machine learning of interatomic potentials, broader data-driven atomistic modelling and the visualisation and analysis of materials datasets. The standard mechanism used to incorporate chemical element information is to create separate densities for each element and form tensor products between them. This leads to a steep scaling in the size of the representation as the number of elements increases. Graph neural networks, which do not explicitly use density representations, escape this scaling by mapping the chemical element information into a fixed dimensional space in a learnable way. We recast this approach as tensor factorisation by exploiting the tensor structure of standard neighbour density based descriptors. In doing so, we form compact tensor-reduced representations whose size does not depend on the number of chemical elements, but remain systematically convergeable and are therefore applicable to a wide range of data analysis and regression tasks.

Over the past decade, machine learning methods for studying atomistic systems have become widely adopted [1–3]. Most of these methods utilise representations of local atomic environments that are invariant under relevant symmetries; typically rotations, reflections, translations and permutations of equivalent atoms [4]. Enforcing these symmetries allows for greater data efficiency during model training and ensures that predictions are made in a physically consistent manner. There are many different ways of constructing such representations which are broadly split into two categories: (i) descriptors based on internal coordinates, such as the Behler-Parrinello Atom-Centered Symmetry Functions [5], and (ii) density-based descriptors such as Smooth Overlap of Atomic Positions (SOAP) [6] or the bispectrum [7, 8], which employ a symmetrised expansion of ν -correlations of the atomic neighbourhood density ($\nu = 2$ for SOAP and $\nu = 3$ for the bispectrum). A major drawback of all these representations is that their size increases dramatically with the number of chemical elements S in the system. For instance, the number of features in the linearly complete Atomic Cluster Expansion (ACE) [9, 10] descriptor, which unifies, extends and generalises the aforementioned representations, scales as S^ν for terms with correlation order ν (i.e. a body order of $\nu + 1$). This poor scaling severely restricts the use of these representations in many applications. For example, in the case of

machine learned interatomic potentials for systems with many (more than 5) different chemical elements, the large size of the models results in memory limitations being reached during parameter estimation as well as significantly reducing evaluation speed.

Multiple strategies to tackle this scaling problem have been proposed including weighting [11, 12] or embedding [13] the elements into a fixed dimensional space, directly reducing the element-sensitive correlation order [14] and data-driven approaches for selecting the most relevant subset or combination of the original features for a given dataset [15–17]. A rather different class of machine learning methods are Message Passing Neural Networks (MPNNs) [18, 19]. Instead of constructing full tensor products, these models embed chemical element information in a fixed size latent space, using a learnable transformation $\mathbb{R}^S \rightarrow \mathbb{R}^K$ where K is the dimension of the latent space, and thus avoid the poor scaling with the number of chemical elements. In recent advances, these methods have achieved very high accuracy [20–22], strongly suggesting that the true complexity of the relevant chemical element space does not grow as S^ν .

In this paper, we introduce a general way to significantly reduce the scaling of the density-based representations like SOAP and ACE with the number of chemical elements. The key idea is to recognise that the parameters of a linear model built on density representations form a symmetric tensor that can be approximated using a symmetric tensor decomposition or a tensor sketch. [23]. We show that the resulting approximation is systematically convergeable to the original full descriptor limit

* These authors contributed equally.

and verify this with numerical experiments on real data. We also show that there is a natural generalisation to compress not only the chemical element information but also the radial degrees of freedom, yielding an even more compact representation. When fitting interatomic potentials for high entropy alloys and organic molecules, we achieve about a ten-fold reduction in the number of features required when using linear (ACE) and nonlinear kernel models (SOAP-GAP).

In the standard linear ACE model, an invariant atomic property (such as the site energy) of atom i , $\varphi_i(Z_i, \{\mathbf{r}_{ij}, Z_j\}_{j \in \mathcal{N}(i)})$, is a function of the local atomic neighbour environment $\mathcal{N}(i) = \{j : r_{ij} < r_{\text{cut}}\}$, where positions and chemical elements are denoted \mathbf{r}_i and Z_i , respectively. The local environments are represented using a complete linear basis in terms of the relative positions \mathbf{r}_{ij} and atomic numbers Z_j of neighbour atoms. First, the one-particle basis is formed as

$$\phi_{znlm}(\mathbf{r}_{ij}, Z_j) = R_n(r_{ij})Y_l^m(\hat{\mathbf{r}}_{ij})\delta_{zZ_j}, \quad (1)$$

where the R_n are orthogonal radial basis functions and the Y_l^m are the standard complex spherical harmonics. The atomic basis is obtained by summing over all neighbours,

$$A_{i,znlm} = \sum_{j \in \mathcal{N}(i)} \phi_{znlm}(\mathbf{r}_{ij}, Z_j), \quad (2)$$

We then take tensor products of the $A_{i,znlm}$ up to order ν to form the product basis

$$\mathbf{A}_{znlm} = \prod_{t=1}^{\nu} A_{i,z_t n_t l_t m_t} \quad (3)$$

where $(\mathbf{z}, \mathbf{n}, \mathbf{l}) = (z_1, n_1, l_1; \dots; z_\nu, n_\nu, l_\nu)$ are lexicographically ordered and for practical applications the basis is truncated using l_{max} , n_{max} and ν_{max} . The product basis is a complete linear basis of $(\nu + 1)$ body-order permutation invariant functions [10]. The rotationally invariant ACE basis is then obtained by symmetrising the product basis with respect to the group $O(3)$,

$$\mathbf{B}_{i,znl\eta} = \sum_{\mathbf{m}} C_{\mathbf{m}}^{znl\eta} \mathbf{A}_{i,znlm} \quad (4)$$

where $C_{\mathbf{m}}^{znl\eta}$ are generalised Clebsch-Gordan coefficients and η simply enumerates all possible symmetric couplings; cf. [9, 10, 15] for the details. The resulting linear ACE model is then

$$\varphi_i = \sum_{znl\eta} c_{znl\eta} \mathbf{B}_{i,znl\eta} \quad (5)$$

where $c_{znl\eta}$ are the model parameters. Due to the tensor product in Eq. (3), the size of the basis (and therefore the number of model parameters) grows rapidly as $S^{\nu_{\text{max}}}$ with the number of chemical elements, S . This explosion

of complexity is contrary to chemical intuition: all atoms exhibit certain basic chemical properties, such as short range repulsion and long range attraction, and there are clear trends across the periodic table in more complex properties such as electronegativity and covalent bonding.

Notice that the parameter set of the linear ACE model, $\mathbf{c} \equiv c_{znl\eta}$, is itself a tensor that is symmetric under a permutation $(z_a, n_a, l_a) \leftrightarrow (z_b, n_b, l_b)$ and so it can be expanded as a sum of products of rank-1 tensors \mathbf{w}_k as

$$\mathbf{c} = \sum_{k=1}^K \lambda_k \underbrace{\mathbf{w}_k \otimes \mathbf{w}_k \cdots \otimes \mathbf{w}_k}_{\nu \text{ times}}. \quad (6)$$

Due to basis truncation, \mathbf{c} is finite, and the expansion in Eq. (6) is exact for sufficiently large but finite K . We approximate the expansion and write it in component form as

$$c_{znl\eta} \approx \sum_k \lambda_{kl\eta} \prod_{t=1}^{\nu} W_{z_t n_t}^{kl_t} \quad (7)$$

where $W_{z_t n_t}^{kl_t}$ are components of \mathbf{w}_k . The approximation in Eq. (7) is due to two reasons: (i) in practice we can achieve excellent accuracy by truncating the sum over k very early, and (ii) we use the same weights for all η and all ν which significantly reduces the number of weights that need to be specified. On the other hand, we generalised the expansion by letting the parameters λ_k become $\lambda_{kl\eta}$ to help accelerate convergence. Note that for $\nu = 2$, \mathbf{c} can be viewed as an array of $(l + 1)$ symmetric matrices $\mathbf{c}_{z_n, z' n'}^l = \mathbf{c}_{z' n', z_n}^l$ and Eq. (6) is equivalent to eigen-decomposition and so is exact for $K = NS$. Substituting Eq. (7) into Eq. (5), using (3)-(4) and reordering the summations, we obtain

$$\varphi_i \approx \sum_{kl\eta} \lambda_{kl\eta} \left[\sum_{\mathbf{m}} C_{\mathbf{m}}^{l\eta} \sum_{\mathbf{z n}} \prod_{t=1}^{\nu} W_{z_t n_t}^{kl_t} A_{i,z_t n_t l_t m_t} \right] \quad (8)$$

$$= \sum_{kl\eta} \lambda_{kl\eta} \tilde{\mathbf{B}}_{i,kl\eta} \quad (9)$$

where we defined new tensor reduced basis functions $\tilde{\mathbf{B}}$ as the expression in brackets, and the model's degrees of freedom are $\lambda_{kl\eta}$. (Note that, the Clebsch-Gordan coupling coefficients now only depend on \mathbf{l} , \mathbf{m} and η .) To facilitate a practical scheme, the tensor reduction can be propagated through the entire ACE construction,

Eqs. (1)-(4), as

$$\tilde{R}_k^l(r_{ij}, Z_j) = \sum_n W_{zn}^{kl} R_n(r_{ij}), \quad (10)$$

$$\tilde{\phi}_{klm}(\mathbf{r}_{ij}, Z_j) = \tilde{R}_k^l(r_{ij}, Z_j) Y_l^m(\hat{\mathbf{r}}_{ij}), \quad (11)$$

$$\tilde{A}_{i,klm} = \sum_{j \in \mathcal{N}(i)} \tilde{\phi}_{klm}(\mathbf{r}_{ij}, Z_j), \quad (12)$$

$$\tilde{\mathbf{A}}_{i,klm} = \prod_{t=1}^{\nu} \tilde{A}_{i,kl_t m_t} \quad (13)$$

$$\tilde{\mathbf{B}}_{i,kl\eta} = \sum_m c_m^{l\eta} \tilde{\mathbf{A}}_{i,klm}. \quad (14)$$

The tensor-reduced ACE basis is thus computed simply by using the modified radial basis functions \tilde{R} . The crucial and novel step is in (13), where the tensor product is not taken over k : we use the K different embedded density projections in an *uncoupled* manner.

The vector indices \mathbf{z} and \mathbf{n} in the original ACE basis have been replaced by the scalar index k , thus eliminating the punishing $\mathcal{O}(N^\nu S^\nu)$ scaling with respect to the number of elements S and number of radial basis functions $N = n_{\max}$. The size of the tensor-reduced basis is instead independent of S and N and scales as $\mathcal{O}(K)$, where the number of embedding channels K is an approximation parameter that controls the level of chemical and radial resolution*. We stress that, because the tensor-reduced basis functions are derived from the tensor-decomposition (6), they remain systematic and still provide a complete basis. Finally, we note that these tensor reduction techniques can be applied to any other quantity entering the one-particle basis, such as a charge, however the angular component of the basis, $Y_l^m(\hat{\mathbf{r}}_{ij})$ must be left untouched. It is also possible to form a partially embedded basis, for instance, by only mixing chemical element channels and leaving the radial portion of the basis unmodified.

The transformation expressed by W_{zn}^{kl} , derived from the symmetric tensor decomposition, is the general form of the embeddings used in refs. 12, 13, 16, 19. There are multiple natural strategies for specifying the embedding weights W_{zn}^{kl} , including approximating a pre-computed $c_{znl\eta}$ or treating the weights as model parameters to be estimated during the training process. The latter approach has been used with success in a number of neural network based models [20–22]. Here, we investigate a simpler alternative: random embedding weights.

Using random weights to compress high-dimensional feature vectors is a well established technique known as

Random Projection (RP) [24, 25], whereby a set of vectors $\{\mathbf{x}_1, \dots, \mathbf{x}_N\} \subset \mathbb{R}^d$ are projected into a lower dimensional space as $\{\tilde{\mathbf{x}}_1, \dots, \tilde{\mathbf{x}}_N\} \subset \mathbb{R}^K$, where $K < d$, $\tilde{\mathbf{x}}_i = \mathbf{W}\mathbf{x}_i$ and the entries of the random matrix \mathbf{W} are normally distributed. This approach is simple, offers a tuneable level of compression and is underpinned by the Johnson-Lindenstrauss (JL) Lemma [26] which bounds the fractional error made in approximating $\mathbf{x}_i^T \mathbf{x}_j$ by $\tilde{\mathbf{x}}_i^T \tilde{\mathbf{x}}_j$.

Random Projection can be used to reduce the cost of linear models. In Compressed Least-Square Regression (CLSR) [27–29] the features are replaced by their projections, thus reducing the number of model parameters. Loosely speaking, the approximation errors incurred in CLSR (and RP in general) are expected to decay as $1/\sqrt{K}$ and we refer to refs. [27, 29, 30] for more details. A closely related idea was recently used to accelerate a kernel based interatomic potential by linearising it via approximating the Gaussian kernel as $\exp(-\gamma|\mathbf{x}_i - \mathbf{x}_j|^2) = \phi_i^T \phi_j \approx \mathbf{z}_i^T \mathbf{z}_j$, where the new features \mathbf{z} are Random Fourier Features [31, 32]. This approximation is analogous to performing Random Projection on the features, ϕ_i , in the Reproducing Kernel Hilbert Space.

The drawback of all these ideas based on RP is that they always require the computation of the full original feature vectors first, and thus would incur the unfavourable $\mathcal{O}(N^\nu S^\nu)$ scaling of the size of the ACE basis. Although the tensor reduction approach shown above is related to RP, it differs in the construction of the compressed features by exploiting the tensor structure of the ACE basis to *avoid ever constructing the original features* and, as such, we have effectively replaced RP with *tensor sketching*[33–35].

The idea behind tensor sketching is that for vectors with tensor structure $\mathbf{x} = \mathbf{y} \otimes \mathbf{z}$ where $\mathbf{x} \in \mathbb{R}^{d_1 d_2}$, $\mathbf{y} \in \mathbb{R}^{d_1}$ and $\mathbf{z} \in \mathbb{R}^{d_2}$, the Random Projection $\mathbf{W}\mathbf{x}$ can be efficiently computed directly from \mathbf{y} and \mathbf{z} as

$$\mathbf{W}\mathbf{x} = \mathbf{W}'\mathbf{y} \circ \mathbf{W}''\mathbf{z}, \quad (15)$$

where \circ denotes the element-wise (Hadamard) product, \mathbf{W}' and \mathbf{W}'' are independent random matrices and there exists a corresponding \mathbf{W} to satisfy this relationship [36]. For our purposes, $\mathbf{x} = \mathbf{A}_{znlm}$ is the product basis from Eq. (3) and $\mathbf{y} = \mathbf{z} = \mathbf{A}_{i,znlm}$ corresponds to the atomic basis from Eq. (2), so that $\mathbf{W}'\mathbf{y} = \tilde{\mathbf{A}}_{i,klm}$ is the embedded atomic basis of Eq. (12) and taking the element-wise product is analogous to only taking the diagonal terms in Eq. (13), rather than a full tensor product.

We make two further observations. First, as defined in Eq. (14), the tensor-reduced basis is not a true tensor sketch because inner products are not preserved under the random projection. More precisely, for any individual

* Note that if a separate model is fitted for each central chemical element, as is common for interatomic potentials, the total number of model parameters would be linear in S . The total evaluation time, however, remains independent of S .

k ,

$$\mathbb{E} \left[\sum_{l\eta} \tilde{\mathbf{B}}_{i,kl\eta} \tilde{\mathbf{B}}_{j,kl\eta} \right] \neq C_0 \sum_{znl\eta} \mathbf{B}_{i,znl\eta} \mathbf{B}_{j,znl\eta}, \quad (16)$$

with C_0 is a constant and independent of i , and the expectation is computed across the distribution of random weights.

However, with a small modification, a different tensor-reduced basis defined as

$$\hat{\mathbf{B}}_{i,kl\eta} = \sum_m C_m^{l\eta} \hat{\mathbf{A}}_{i,klm} \quad (17)$$

$$\hat{\mathbf{A}}_{i,klm} = \prod_{t=1}^{\nu} \tilde{\mathbf{A}}_{i,k_t l_t m_t} \quad (18)$$

does preserve inner products; see the Supporting Information for details. The key modification is to use independently chosen tuples $\mathbf{k} = (k_1, k_2, \dots, k_\nu)$, rather than a single k , to construct $\hat{\mathbf{A}}_{i,klm}$. This choice corresponds to $\mathbf{W}' \neq \mathbf{W}''$ in Eq. (15) so that this construction is a true tensor sketch.

The drawback of this is that ν times more embedded radial channels are needed compared with (10)–(14) for each final many-body basis function, so that $\hat{\mathbf{B}}$ is more expensive to evaluate. Finally, we note that because the embedded channels are independent, the error in approximating inner products using the average across K channels is expected to decrease as $1/\sqrt{K}$, just as with standard RP. Based on this, we conjecture that similar bounds derived for the errors made in CLSR may also apply here.

We now turn to numerical results and first demonstrate that the tensor-reduced features are able to efficiently and completely describe a many-element training set. Consider a dataset comprised of all symmetry inequivalent fcc structures made of up of 5 elements with up to 6 atoms per unit cell [37]. A set of features is complete on this dataset if the design matrix for a linear model fit to total energies has full (numerical) row rank, where each row corresponds to a different training configuration.

Figure 1 shows the numerical rank of the design matrix as a function of the basis set. At a given correlation the standard ACE basis set is grown by increasing the polynomial degree, and the tensor-reduced basis set is enlarged by increasing K , the number of independent channels. In both cases once the rank stops increasing at the given correlation order we increment the latter. The colors in Fig. 1 correspond to three different geometrical variations: blue contains on-lattice configurations only whilst in magenta and red the atomic positions have been perturbed by a random Gaussian displacement with mean 0 and standard deviation of 0.025 and 0.25 Å, respectively. The dotted lines corresponds to the standard ACE basis, whereas the solid lines corresponds to the

tensor-reduced version from Eq. (14). Although the standard ACE basis can always achieve full row rank since it is a complete linear basis, it does this very inefficiently. In contrast, the row rank of the tensor-reduced basis grows almost linearly. Thus the tensor-reduced basis, having removed unnecessary redundancies, still retains the expressive power of the full basis.

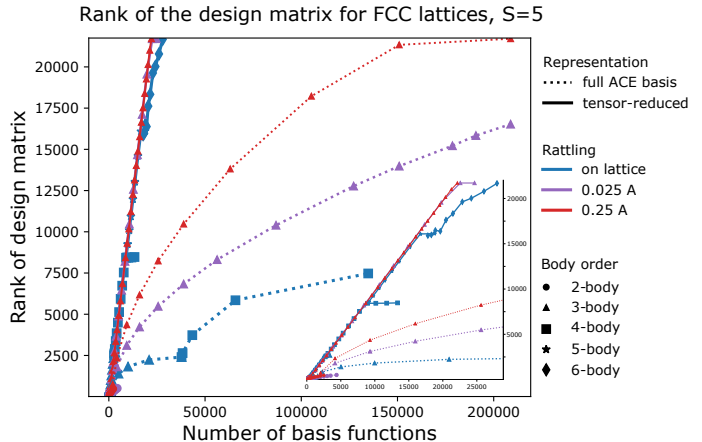


FIG. 1. The rank of the design matrix as a function of basis set on a dataset of all symmetry inequivalent fcc lattices of 5 chemical elements and unit cell sizes of up to 6 atoms. Both in the case of on-lattice and rattled geometries the tensor-reduced ACE basis reaches full numerical rank in a nearly ideal ($x = y$) way. This is in contrast to standard ACE where the rank is increasing slowly as the new basis functions are added. The inset zooms in on the $x = y$ region.

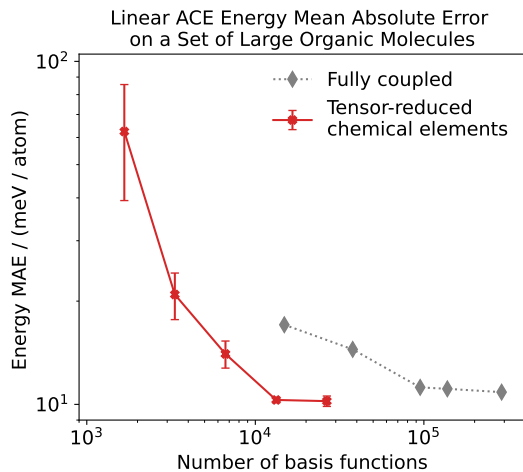


FIG. 2. Convergence of the energy errors on the independent test set with respect to the number of basis functions is shown for a linear Tensor-reduced ACE model and a standard linear ACE model. Error bars show the standard error in the mean, computed across 5 fits using independently chosen random weights

Next, we fit a linear ACE [38] model on a training set of 400 different organic molecules of size 19-168 atoms,

randomly selected from the QMugs dataset [39] that are made up of 10 different chemical elements (H, C, N, O, F, P, S, Cl, Br, I). The conformers were created by running GFN2-xTB [40] 800 K NVT molecular dynamics for 1 ps starting from a published minimum energy structure. The test set is composed of 1,000 *different* molecules sampled the same way. This is a small-data regime task that is particularly challenging due to the chemical and conformational diversity. Figure 2 shows the convergence of the energy error with the number of basis functions for the fully coupled and the tensor-reduced ACE models, both using $\nu_{\max} = 3$ (4-body). By increasing the number of uncoupled channels K we can converge the accuracy to the previous level, whilst reducing the size of the model by a factor of 10.

Next, we investigate tensor-reduced forms of the SOAP power spectrum. The information imbalance, introduced in ref. [41], provides a quantitative way to measure the relative information content of descriptors by comparing the pairwise distances between atomic environments in a given dataset. For a given environment, all other environments in the dataset are ranked (denoted by r) according to their distance from it using two different descriptors A and B . The information imbalance is then defined as

$$\Delta_{B \rightarrow A} = \frac{2}{n_{\text{env}}} \langle r_B | r_A = 1 \rangle \quad (19)$$

where $r_B | r_A = 1$ is the rank according to B of the nearest neighbour according to A and the average $\langle r_B | r_A = 1 \rangle$ is across all n_{env} environments in the dataset. Defined as such, for large n_{env} , $\Delta_{B \rightarrow A} \approx 0$ when B contains the same information as A and $\Delta_{B \rightarrow A} \approx 1$ if B contains no information about A . By using nearest neighbour information, $\Delta_{B \rightarrow A}$ is sensitive only to the local neighbourhood around a given data point and is insensitive to any scaling of the distances, making it well suited to study non-linear relationships between different distance measures.

In applying the tensor reduction formalism to SOAP, we switch to its customary notation, i.e. \mathbf{c}_{nl}^z is the neighbour density expansion (playing the role of the atomic basis A of ACE) and $p_{nn'l}^{zz'} = \mathbf{c}_{nl}^z \cdot \mathbf{c}_{n'l}^{z'}$ for the power spectrum (corresponding to the product basis \mathbf{A} in ACE for $\nu = 2$, where the Clebsch-Gordan coefficients are all 1)[42]. In Fig. 3 the information imbalance between the full SOAP power spectrum and various tensor-reduced forms is shown as a function of descriptor length for a dataset of high-entropy alloy liquid environments containing 5 elements. New mixed element channels are constructed by randomly mixing element densities and denoted as $\tilde{\mathbf{c}}_{nl}^k = \sum_z w_z^k \mathbf{c}_{nl}^z$ whilst mixed element-radial channels are denoted as $\hat{\mathbf{c}}_l^k = \sum_{zn} w_{zn}^k \mathbf{c}_{nl}^z$. Mixing element and radial channels together $p_l^{kq} = \hat{\mathbf{c}}_l^k \cdot \hat{\mathbf{c}}_l^q$ (dotted blue) leads to a higher information content than mixing element channels $p_{nn'l}^{kq} = \tilde{\mathbf{c}}_{nl}^k \cdot \tilde{\mathbf{c}}_{n'l}^q$ alone (dotted red). Similarly, not coupling the mixed channels

together (solid) outperforms coupling them (dotted) for both types of mixing, with uncoupled element-radial mixing $p_l^k = \hat{\mathbf{c}}_l^k \cdot \hat{\mathbf{c}}_l^k$, as in Eq. (9), being the best combination. We also note that using $p_l^k = \hat{\mathbf{c}}_l^{k_1} \cdot \hat{\mathbf{c}}_l^{k_2}$, see Eq. (18), marginally outperforms p_l^k on this test, which is expected as p_l^k provides an unbiased estimator for the reference distances. A random projection [24–26] of $p_{nn'l}^{zz'}$ (black dashed) and $p_{nn'l}^{zz'}$ itself simply computed using fewer basis functions (grey dotted), were also included as references. Notably, using the fully tensor-reduced power spectrum provides comparable performance to random projection whilst avoiding constructing the full $p_{nn'l}^{zz'}$ as an intermediate step. Details of the SOAP parameters and equivalent results for the revised MD17 [43] dataset and a single element phosphorous dataset [44] are included in the Supporting Information.

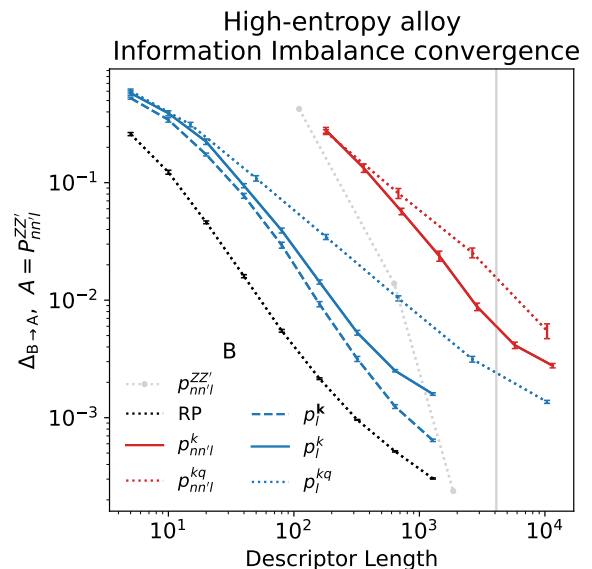


FIG. 3. Convergence of the information imbalance, relative to the full power spectrum, for 1000 randomly chosen environments from liquid configurations in a high-entropy alloy dataset [45], $S=5$. Element and element-radial mixing are indicated using red and blue respectively. Fully coupled channels are indicated with a dotted line whilst uncoupled channels are indicated with a solid (or dashed) line. The black dotted line corresponds to a random projection of the full power spectrum whilst the grey dotted line corresponds to $p_{nn'l}^{zz'}$ computed using fewer basis functions (while keeping the $n_{\max} = 2l_{\max}$ relation). Error bars show the standard error in the mean across 10 randomly chosen sets of weights and the vertical grey line indicates the length of the reference power spectrum, $n_{\max} = 8, l_{\max} = 4$.

We used the tensor-reduced SOAP descriptor to fit Gaussian Approximation Potential (GAP) [7] models to the high-entropy alloy dataset from ref. [45]. The descriptors were computed using turbo-soap [46] and fitting was performed using the GAP code [47]. To provide a

baseline for comparison, reference models were fit using the full power spectrum evaluated with a varying number of basis functions; $n_{\max} = 2l_{\max}$. All compressed descriptors were constructed using the largest values of $n_{\max} = 8, l_{\max} = 4$ and all models used a polynomial kernel with $\zeta = 6$, see Supporting Information for full details. The force errors achieved on the independent test set are shown as a function of descriptor length in Fig. 4. For this dataset, mixing only the chemical elements did not help, which is likely due to the minimal savings made as a result of the low correlation order. However, using the fully element-radial tensor-reduced descriptor allowed for similar accuracy to be achieved using approximately ten times fewer SOAP features. Furthermore, the errors achieved with all compressed descriptors can be seen to converge towards those achieved with the full SOAP vector they are derived from. Finally, in the high accuracy regime, with descriptor lengths of 250 or higher, models fit using p_l^k matched the accuracy achieved using full RP. This is a particularly promising result since bypassing the need to construct the full power spectrum as an intermediate step allows for faster potential evaluation.

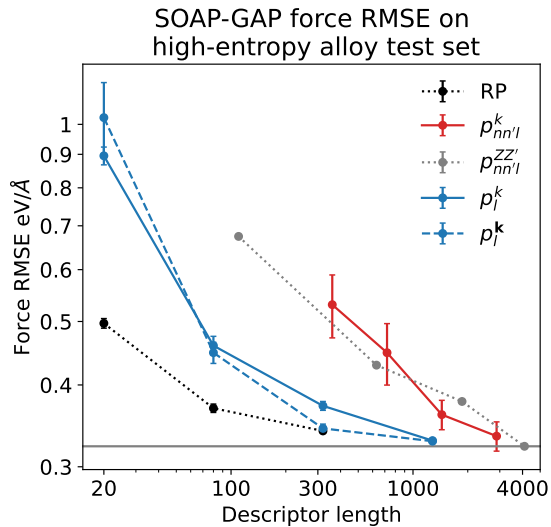


FIG. 4. Convergence of force RMSE on the high-entropy alloy test set as a function of descriptor length for various GAP models, $\zeta = 6$. The dotted grey line is full SOAP using $n_{\max} = 2l_{\max}$, for $l_{\max} = 1, 2, 3, 4$. The dotted black line is a random projection of the full power spectrum whilst the red and blue lines use tensor-reduced features with element and element-radial mixing respectively. Error bars show the standard error in the mean, computed across 5 fits using independently chosen random weights.

Finally, we assess the effect of optimising the embedding weights in the tensor-reduced basis using the MACE architecture [22]. A typical MACE model is a 2-layer message passing network which utilises the uncoupled ACE basis to efficiently represent equivariant body-ordered messages. Normally, the embedding

weights are optimised using backpropagation along with all other model parameters as usual with network models, but it is possible to fix these weights to random values. Whilst a multi-layer MACE is a complex non-linear network model, a single-layer MACE with frozen embedding weights is equivalent to a linear ACE model with a fully uncoupled basis [21].

We use the HME21 dataset [48, 49] for this test due to its exceptional diversity, both chemically with 45 elements, and structurally with configurations including isolated molecules, bulk crystals, surfaces, clusters and disordered materials. We fit several models (see the Supporting Information for details), and the energy and force errors on the independent test set are summarised in Table I. Strikingly, using random element embedding weights leads to almost no degradation in model accuracy compared to using optimised weights. In contrast, we found that using random embedding weights for the tensor reduction of both chemical and radial indices lead to significantly larger prediction errors. A two-layer model with optimised weights achieves state of the art accuracy on HME21, showing the power of the message passing architecture and further highlighting the effectiveness of the uncoupled basis.

TABLE I. Mean absolute errors on the HME21 dataset. Energy (E , meV) and force (F , eV/Å) errors of models. The labels, (1) or (2), of the MACE models indicate the number of message passing layers.

	MACE (1) element-only random	MACE (1) element-radial optimised	MACE (2) element-radial optimised	TeaNet [50]	NequIP [20]
E	53.5	52.1	15.7	19.6	47.8
F	0.189	0.175	0.138	0.174	0.199

In conclusion, we introduced a tensor-reduced form of the ACE basis for modelling symmetric functions of local atomic neighbour environments that eliminates the $\mathcal{O}(N^\nu S^\nu)$ scaling of the basis set size with the number of chemical elements and radial basis functions. Intuitively, the construction can be thought of as mixing the element and radial channels and then only coupling these channels to themselves when constructing the higher order many-body basis. We derived this new embedded basis from a symmetric tensor decomposition and explored its connection to tensor-sketching. We showed that this reduced basis is also systematic, and that in practice it can enable a 10-fold reduction in basis set size for diverse datasets with many elements, including organic molecules and high entropy alloys.

DPK acknowledges support from AstraZeneca and the EPSRC. GC acknowledges discussion with Boris Kozinsky. JPD and GC acknowledge support from the NOMAD Centre of Excellence, funded by the European Commission under grant agreement 951786. We used computational resources of the UK HPC service

ARCHER2 via the UKCP consortium and funded by EP-SRC grant EP/P022596/1. CO acknowledges support of the Natural Sciences and Engineering Research Council [Discovery Grant IDGR019381] and the New Frontiers in Research Fund [Exploration Grant GR022937].

-
- [1] V. L. Deringer, N. Bernstein, G. Csányi, C. Ben Mahmoud, M. Ceriotti, M. Wilson, D. A. Drabold, and S. R. Elliott, Origins of structural and electronic transitions in disordered silicon, *Nature* **589**, 59 (2021).
- [2] T. A. Young, T. Johnston-Wood, H. Zhang, and F. Duarte, Reaction dynamics of diels-alder reactions from machine learned potentials, *Phys. Chem. Chem. Phys.* **24**, 20820 (2022).
- [3] V. Kapil, C. Schran, A. Zen, J. Chen, C. J. Pickard, and A. Michaelides, The first-principles phase diagram of monolayer nanoconfined water, *Nature* **609**, 512–516 (2022).
- [4] F. Musil, A. Grisafi, A. P. Bartók, C. Ortner, G. Csányi, and M. Ceriotti, Physics-inspired structural representations for molecules and materials, *Chemical Reviews* **121**, 9759 (2021).
- [5] J. Behler and M. Parrinello, Generalized neural-network representation of high-dimensional potential-energy surfaces, *Phys. Rev. Lett.* **98**, 146401 (2007).
- [6] A. P. Bartók, R. Kondor, and G. Csányi, On representing chemical environments, *Physical Review B* **87**, 184115 (2013).
- [7] A. P. Bartók, M. C. Payne, R. Kondor, and G. Csányi, Gaussian approximation potentials: The accuracy of quantum mechanics, without the electrons, *Physical review letters* **104**, 136403 (2010).
- [8] A. Thompson, L. Swiler, C. Trott, S. Foiles, and G. Tucker, Spectral neighbor analysis method for automated generation of quantum-accurate interatomic potentials, *Journal of Computational Physics* **285**, 316 (2015).
- [9] R. Drautz, Atomic cluster expansion for accurate and transferable interatomic potentials, *Phys. Rev. B* **99**, 014104 (2019).
- [10] G. Dusson, M. Bachmayr, G. Csányi, R. Drautz, S. Etter, C. van der Oord, and C. Ortner, Atomic cluster expansion: Completeness, efficiency and stability, *Journal of Computational Physics* **454**, 110946 (2022).
- [11] M. Gastegger, L. Schwiedrzik, M. Bittermann, F. Berzsenyi, and P. Marquetand, wacsf—weighted atom-centered symmetry functions as descriptors in machine learning potentials, *The Journal of chemical physics* **148**, 241709 (2018).
- [12] N. Artrith, A. Urban, and G. Ceder, Efficient and accurate machine-learning interpolation of atomic energies in compositions with many species, *Physical Review B* **96**, 014112 (2017).
- [13] M. J. Willatt, F. Musil, and M. Ceriotti, Feature optimization for atomistic machine learning yields a data-driven construction of the periodic table of the elements, *Physical Chemistry Chemical Physics* **20**, 29661 (2018).
- [14] J. P. Darby, J. R. Kermode, and G. Csányi, Compressing local atomic neighbourhood descriptors, *npj Computational Materials* **8**, 1 (2022).
- [15] J. Nigam, S. Pozdnyakov, and M. Ceriotti, Recursive evaluation and iterative contraction of n-body equivariant features, *The Journal of Chemical Physics* **153**, 121101 (2020), <https://doi.org/10.1063/5.0021116>.
- [16] A. Goscinski, F. Musil, S. Pozdnyakov, J. Nigam, and M. Ceriotti, Optimal radial basis for density-based atomic representations, *The Journal of Chemical Physics* **155**, 104106 (2021).
- [17] C. Zeni, K. Rossi, A. Glielmo, and S. De Gironcoli, Compact atomic descriptors enable accurate predictions via linear models, *The Journal of Chemical Physics* **154**, 224112 (2021).
- [18] J. Gilmer, S. S. Schoenholz, P. F. Riley, O. Vinyals, and G. E. Dahl, Neural message passing for quantum chemistry (2017).
- [19] K. Schütt, P.-J. Kindermans, H. E. Sauceda Felix, S. Chmiela, A. Tkatchenko, and K.-R. Müller, SchNet: A continuous-filter convolutional neural network for modeling quantum interactions, in *Advances in Neural Information Processing Systems*, Vol. 30, edited by I. Guyon, U. V. Luxburg, S. Bengio, H. Wallach, R. Fergus, S. Vishwanathan, and R. Garnett (Curran Associates, Inc., 2017).
- [20] S. Batzner, A. Musaelian, L. Sun, M. Geiger, J. P. Mailoa, M. Kornbluth, N. Molinari, T. E. Smidt, and B. Kozinsky, E(3)-equivariant graph neural networks for data-efficient and accurate interatomic potentials, *Nature Communications* **13**, 2453 (2022).
- [21] I. Batatia, S. Batzner, D. P. Kovács, A. Musaelian, G. N. C. Simm, R. Drautz, C. Ortner, B. Kozinsky, and G. Csányi, The design space of e(3)-equivariant atom-centered interatomic potentials (2022).
- [22] I. Batatia, D. P. Kovács, G. N. C. Simm, C. Ortner, and G. Csányi, Mace: Higher order equivariant message passing neural networks for fast and accurate force fields (2022).
- [23] D. P. Woodruff *et al.*, Sketching as a tool for numerical linear algebra, *Foundations and Trends® in Theoretical Computer Science* **10**, 1 (2014).
- [24] S. Dasgupta, Experiments with random projection, arXiv preprint arXiv:1301.3849 (2013).
- [25] E. Bingham and H. Mannila, Random projection in dimensionality reduction: applications to image and text data, in *Proceedings of the seventh ACM SIGKDD international conference on Knowledge discovery and data mining* (2001) pp. 245–250.
- [26] W. B. Johnson, Extensions of lipschitz mappings into a hilbert space, *Contemp. Math.* **26**, 189 (1984).
- [27] A. Kabán, A new look at compressed ordinary least squares, in *2013 IEEE 13th International Conference on Data Mining Workshops* (IEEE, 2013) pp. 482–488.
- [28] S. E. Ahmed, *Big and complex data analysis: methodologies and applications* (Springer, 2017).
- [29] O. Maillard and R. Munos, Compressed least-squares regression, *Advances in neural information processing systems* **22** (2009).
- [30] D. Hsu, S. M. Kakade, and T. Zhang, Random design analysis of ridge regression, in *Conference on learning theory* (JMLR Workshop and Conference Proceedings, 2012) pp. 9–1.
- [31] N. J. Browning, F. A. Faber, and O. A. von Lilienfeld, Gpu-accelerated approximate kernel method for quantum machine learning, arXiv preprint arXiv:2206.01580 (2022).

- [32] A. Rahimi and B. Recht, Random features for large-scale kernel machines, *Advances in neural information processing systems* **20** (2007).
- [33] Y. Liu, J. Liu, Z. Long, and C. Zhu, *Tensor computation for data analysis* (Springer, 2022).
- [34] R. Pagh, Compressed matrix multiplication, *ACM Transactions on Computation Theory (TOCT)* **5**, 1 (2013).
- [35] N. Pham and R. Pagh, Fast and scalable polynomial kernels via explicit feature maps, in *Proceedings of the 19th ACM SIGKDD international conference on Knowledge discovery and data mining* (2013) pp. 239–247.
- [36] T. D. Ahle and J. B. Knudsen, Almost optimal tensor sketch, arXiv preprint arXiv:1909.01821 (2019).
- [37] G. L. Hart and R. W. Forcade, Algorithm for generating derivative structures, *Physical Review B* **77**, 224115 (2008).
- [38] D. P. Kovács, C. v. d. Oord, J. Kucera, A. E. A. Allen, D. J. Cole, C. Ortner, and G. Csányi, Linear atomic cluster expansion force fields for organic molecules: Beyond rmse, *Journal of Chemical Theory and Computation* **17**, 7696 (2021), pMID: 34735161, <https://doi.org/10.1021/acs.jctc.1c00647>.
- [39] C. Isert, K. Atz, J. Jiménez-Luna, and G. Schneider, Qmugs, quantum mechanical properties of drug-like molecules, *Scientific Data* **9**, 1 (2022).
- [40] C. Bannwarth, S. Ehlert, and S. Grimme, Gfn2-xtb—an accurate and broadly parametrized self-consistent tight-binding quantum chemical method with multipole electrostatics and density-dependent dispersion contributions, *Journal of chemical theory and computation* **15**, 1652 (2019).
- [41] A. Glielmo, C. Zeni, B. Cheng, G. Csányi, and A. Laio, Ranking the information content of distance measures, *PNAS Nexus* 10.1093/pnasnexus/pgac039 (2022).
- [42] V. L. Deringer, A. P. Bartók, N. Bernstein, D. M. Wilkins, M. Ceriotti, and G. Csányi, Gaussian process regression for materials and molecules, *Chemical Reviews* **121**, 10073 (2021), pMID: 34398616, <https://doi.org/10.1021/acs.chemrev.1c00022>.
- [43] A. S. Christensen and O. A. Von Lilienfeld, On the role of gradients for machine learning of molecular energies and forces, *Machine Learning: Science and Technology* **1**, 045018 (2020).
- [44] V. L. Deringer, M. A. Caro, and G. Csányi, A general-purpose machine-learning force field for bulk and nanostructured phosphorus, *Nature communications* **11**, 1 (2020).
- [45] J. Byggmästar, K. Nordlund, and F. Djurabekova, Modeling refractory high-entropy alloys with efficient machine-learned interatomic potentials: Defects and segregation, *Physical Review B* **104**, 104101 (2021).
- [46] M. A. Caro, Optimizing many-body atomic descriptors for enhanced computational performance of machine learning based interatomic potentials, *Physical Review B* **100**, 024112 (2019).
- [47] github.com/libatoms/gap.
- [48] S. Takamoto, C. Shinagawa, D. Motoki, K. Nakago, W. Li, I. Kurata, T. Watanabe, Y. Yayama, H. Iriguchi, Y. Asano, T. Onodera, T. Ishii, T. Kudo, H. Ono, R. Sawada, R. Ishitani, M. Ong, T. Yamaguchi, T. Kataoka, A. Hayashi, N. Charoenphakdee, and T. Ibuka, High-temperature multi-element 2021 (HME21) dataset (2022).
- [49] S. Takamoto, C. Shinagawa, D. Motoki, K. Nakago, W. Li, I. Kurata, T. Watanabe, Y. Yayama, H. Iriguchi, Y. Asano, *et al.*, Towards universal neural network potential for material discovery applicable to arbitrary combination of 45 elements, *Nature Communications* **13**, 1 (2022).
- [50] S. Takamoto, S. Izumi, and J. Li, TeaNet: Universal neural network interatomic potential inspired by iterative electronic relaxations, *Computational Materials Science* **207**, 111280 (2022).

SUPPORTING INFORMATION

Symmetric Tensor Decomposition of $c_{znl\eta}$

We start by relabelling the parameter tensor $c_{znl\eta}$ of Eq. (5) to $c_{nl\eta}$ where the element index has been incorporated into $\mathbf{n} = ((z_1, n_1), (z_2, n_2), \dots, (z_\nu, n_\nu))$. Then we remove the lexicographical ordering of $(z, \mathbf{n}, \mathbf{l})$ and retain **all** terms in the tensor-product so that there are redundancies in $\mathbf{B}_{i, \mathbf{n}l\eta}$. The advantage of this is that the generalised Clebsch-Gordon coefficients do not depend on \mathbf{n} , which simplifies this analysis. Next we note that $c_{nl\eta}$ is symmetric under $(n_i, l_i) \leftrightarrow (n_j, l_j)$, but not $n_i \leftrightarrow n_j$ or $l_i \leftrightarrow l_j$. We can now use the fact that a symmetric tensor can be expanded in terms of rank-1 tensors, i.e.

$$\mathbf{c} = \sum_k \lambda_k \mathbf{w}^k \otimes \mathbf{w}^k \otimes \dots \otimes \mathbf{w}^k \quad (20)$$

or, rewritten in component form,

$$c_{nl\eta} \sim \sum_k^K \lambda_{k\eta} [\mathbf{w}^k]_{n_1}^{l_1} \dots [\mathbf{w}^k]_{n_\nu}^{l_\nu} \quad (21)$$

where the components of \mathbf{w}^k are indexed with the tuple (n_i, l_i) as $[\mathbf{w}^k]_{n_i}^{l_i} = w_{n_i}^{kl_i}$. Note that the same set of \mathbf{w}^k are used to expand all $c_{nl\eta}$, rather than having a separate set for each (\mathbf{l}, η) tuple. Consequently the expansion for each (\mathbf{l}, η) will converge slower, although we stress that it is still systematic, but crucially we require far fewer embedded one particle basis functions. We then insert this expression into

$$\varphi = \sum_{lm\eta} C_{lm}^\eta \sum_{\mathbf{n}} c_{nl\eta} \mathbf{A}_{nlm}. \quad (22)$$

and get

$$\sum_{\mathbf{n}} c_{nl\eta} \mathbf{A}_{nlm} = \sum_{\mathbf{n}} \sum_k \lambda_{k\eta} \prod_{t=1}^{\nu} w_{n_t}^{kl_t} A_{n_t l_t m_t} \quad (23)$$

$$= \sum_k \lambda_{k\eta} \sum_{\mathbf{n}} \prod_{t=1}^{\nu} w_{n_t}^{kl_t} A_{n_t l_t m_t} \quad (24)$$

$$= \sum_k \lambda_{k\eta} \prod_{t=1}^{\nu} \sum_n w_n^{kl_t} A_{nl_t m_t} \quad (25)$$

$$= \sum_k \lambda_{k\eta} \prod_{t=1}^{\nu} \tilde{A}_{k, l_t, m_t} \quad (26)$$

where

$$\tilde{A}_{k, l_t, m_t} = \sum_n w_n^{kl_t} A_{nl_t k_t} \quad (27)$$

$$= \sum_n w_n^{kl_t} \sum_j R_{nl_t}(r_j) Y_{l_t}^{m_t}(\hat{\mathbf{r}}_j) \quad (28)$$

$$= \sum_j \left[\sum_n w_n^{kl_t} R_{nl_t}(r_j) \right] Y_{l_t}^{m_t}(\hat{\mathbf{r}}_j) \quad (29)$$

$$=: \sum_j \tilde{R}_{kl_t}(r_j) Y_{l_t}^{m_t}(\hat{\mathbf{r}}_j). \quad (30)$$

and $\tilde{R}_{kl_t}(r_j) = \sum_n w_n^{kl_t} R_{nl_t}(r_j)$ is a mixed element-radial basis function. Subbing Eq. (30) back into Eq. (22) we arrive at

$$\varphi = \sum_{k\eta} \lambda_{k\eta} \tilde{\mathbf{B}}_{k\eta} \quad (31)$$

$$\tilde{\mathbf{B}}_{k\eta} = \sum_{lm} C_{lm}^\eta \tilde{\mathbf{A}}_{klm}, \quad (32)$$

$$\tilde{\mathbf{A}}_{klm} = \prod_t \tilde{\mathbf{A}}_{kl_t m_t}. \quad (33)$$

Where each basis function $\tilde{\mathbf{B}}_{k\eta}$ involves a sum over all \mathbf{l} tuples at the given correlation order. An alternative option is to decompose $c_{nl\eta}$ approximately as

$$c_{nl\eta} \sim \sum_k^{k_{\max}} \lambda_{kl\eta} [\mathbf{w}^{kl_1}]_{n_1} \cdots [\mathbf{w}^{kl_\nu}]_{n_\nu}, \quad (34)$$

where the difference is that $[\mathbf{w}^{kl_i}]_{n_i} \rightarrow [\mathbf{w}^{kl_i}]_{n_i}$. Proceeding as above results in the identical analysis as before, except that now the basis functions become

$$\varphi = \sum_{kl} \lambda_{kl\eta} \tilde{\mathbf{B}}_{kl\eta} \quad (35)$$

$$\tilde{\mathbf{B}}_{kl\eta} = \sum_m C_{lm}^\eta \tilde{\mathbf{A}}_{klm} \quad (36)$$

and $\tilde{\mathbf{A}}_{klm}$ is as above. Both are valid expansions and comparing Eq. (32) and Eq. (36) we see that $\tilde{\mathbf{B}}_{k\eta} = \sum_l \tilde{\mathbf{B}}_{kl\eta}$. In this work we choose to investigate using $\tilde{\mathbf{B}}_{kl\eta}$ as every computed $\tilde{\mathbf{B}}_{kl\eta}$ is used separately, so that the model is more flexible for a similar evaluation cost. We note that using $\tilde{\mathbf{B}}_{k\eta}$ might result in a greater level of model accuracy for a given basis set size but leave this investigation to future work.

Uncoupled Basis as a Tensor Sketch

Here we investigate whether inner products are preserved when moving from the full ACE basis to the uncoupled basis. Precisely, we investigate whether $\sum_{l\eta} \tilde{\mathbf{B}}_{i,kl\eta} \tilde{\mathbf{B}}_{j,kl\eta}$ from Eq. (14) and $\sum_{l\eta} \hat{\mathbf{B}}_{i,kl\eta} \hat{\mathbf{B}}_{j,kl\eta}$ from Eq. (18) are unbiased estimators for $\sum_{znl\eta} \mathbf{B}_{i,znl\eta} \mathbf{B}_{j,znl\eta}$ from Eq. (5) when the weights W_{zn}^{kl} are drawn from a symmetric distribution with mean 0. We start by combining the element and radial indices so that $\mathbf{B}_{znl\eta} \rightarrow \mathbf{B}_{nl\eta}$. First we note that

$$\sum_{nl\eta} \mathbf{B}_{i,nl\eta} \mathbf{B}_{j,nl\eta} = \sum_{nl\eta} \left(\sum_m C_{lm}^\eta \mathbf{A}_{i,nlm} \right) \left(\sum_{m'} C_{lm'}^\eta \mathbf{A}_{j,nlm'} \right) \quad (37)$$

$$= \sum_{lmm'\eta} C_{lm}^\eta C_{lm'}^\eta \left(\sum_n \mathbf{A}_{i,nlm} \mathbf{A}_{j,nlm'} \right) \quad (38)$$

and similarly

$$\sum_{kl\eta} \hat{\mathbf{B}}_{i,kl\eta} \hat{\mathbf{B}}_{j,kl\eta} = \sum_{kl\eta} \left(\sum_m C_{lm}^\eta \hat{\mathbf{A}}_{i,klm} \right) \left(\sum_{m'} C_{lm'}^\eta \hat{\mathbf{A}}_{j,klm'} \right) \quad (39)$$

$$= \sum_{lmm'\eta} C_{lm}^\eta C_{lm'}^\eta \left(\sum_k \hat{\mathbf{A}}_{i,klm} \hat{\mathbf{A}}_{j,klm'} \right) \quad (40)$$

where the sum over \mathbf{k} is over randomly chosen tuples (k_1, k_2, \dots, k_ν) where $k_i \neq k_j$. Comparing Eq. (38) and Eq. (40) we see that it is sufficient to check that

$$\sum_{\mathbf{k}} \mathbb{E}[\hat{\mathbf{A}}_{i,klm} \hat{\mathbf{A}}_{j,klm'}] = \sum_{\mathbf{n}} \mathbf{A}_{i,nlm} \mathbf{A}_{j,nlm'} \quad (41)$$

Next we note that every \mathbf{k} tuple is independent, so we need only check one term in the sum on the left. Inserting the definition of $\hat{\mathbf{A}}_{\mathbf{k}lm}$ we find that

$$\hat{\mathbf{A}}_{i,\mathbf{k}lm} \hat{\mathbf{A}}_{j,\mathbf{k}lm'} = \prod_t^\nu \tilde{A}_{i,l_t m_t}^{k_t} \tilde{A}_{j,l_t m'_t}^{k_t} \quad (42)$$

$$= \prod_t^\nu \left(\sum_n W_n^{k_t l_t} A_{i,n l_t m_t} \right) \left(\sum_{n'} W_{n'}^{k_t l_t} A_{j,n' l_t m'_t} \right) \quad (43)$$

$$= \sum_{\mathbf{nn}'} \prod_t^\nu W_{n_t}^{k_t l_t} W_{n'_t}^{k_t l_t} A_{i,n_t l_t m_t} A_{j,n'_t l_t m'_t} \quad (44)$$

$$= \sum_{\mathbf{nn}'} \prod_t^\nu A_{i,n_t l_t m_t} A_{j,n'_t l_t m'_t} \prod_t^\nu W_{n_t}^{k_t l_t} W_{n'_t}^{k_t l_t} \quad (45)$$

$$(46)$$

Next we take the expectation value

$$\mathbb{E} \left[\hat{\mathbf{A}}_{i,\mathbf{k}lm} \hat{\mathbf{A}}_{j,\mathbf{k}lm'} \right] = \sum_{\mathbf{nn}'} \prod_t^\nu A_{i,n_t l_t m_t} A_{j,n'_t l_t m'_t} \mathbb{E} \left[\prod_t^\nu W_{n_t}^{k_t l_t} W_{n'_t}^{k_t l_t} \right] \quad (47)$$

$$= \sum_{\mathbf{nn}'} \prod_t^\nu A_{i,n_t l_t m_t} A_{j,n'_t l_t m'_t} \mathbb{E} [W^2]^\nu \delta_{\mathbf{nn}'} \quad (48)$$

$$= \mathbb{E} [W^2]^\nu \sum_{\mathbf{n}} \prod_t^\nu A_{i,n_t l_t m_t} A_{j,n_t l_t m'_t} \quad (49)$$

$$= \mathbb{E} [W^2]^\nu \sum_{\mathbf{n}} \mathbf{A}_{i,\mathbf{n}lm} \mathbf{A}_{j,\mathbf{n}lm} \quad (50)$$

where $\mathbb{E} [W_{n_i}^{k_i l_i} W_{n'_i}^{k_i l'_i}] = \delta_{k_i k'_i} \delta_{l_i l'_i} \delta_{n_i n'_i} \mathbb{E} [W^2]$ because the $W_{n_i}^{k_i l_i}$ are i.i.d. random variables with mean 0. Eq. (50) is the result we require, up to a constant factor of $\mathbb{E} [W^2]^\nu$ which can be absorbed into the definition of $\tilde{\mathbf{B}}_{\mathbf{k}l\eta}$.

The analysis for $\tilde{\mathbf{B}}_{\mathbf{k}l\eta}$ follows in the same way except that we have $\mathbb{E} \left[\prod_i^\nu W_{n_i}^{k_i l_i} W_{n'_i}^{k_i l'_i} \right] \rightarrow \mathbb{E} \left[\prod_i^\nu W_{n_i}^{k_i l_i} W_{n'_i}^{k_i l_i} \right]$ in Eq. (48). If all l_i in \mathbf{l} are unique then $\mathbb{E} \left[\prod_i^\nu W_{n_i}^{k_i l_i} W_{n'_i}^{k_i l_i} \right] = \prod_i^\nu \mathbb{E} [W^2] \delta_{n_i n'_i}$. However if any of the l_i are repeated then there are additional terms which adjust the expectation value e.g. $\mathbf{l} = (2, 3, 2)$,

$$\mathbb{E} \left[W_{n_1}^{k,2} W_{n'_1}^{k,2} \cdot W_{n_2}^{k,3} W_{n'_2}^{k,3} \cdot W_{n_3}^{k,2} W_{n'_3}^{k,2} \right] = \quad (51)$$

$$\mathbb{E}[W^2]^3 (\delta_{n_1 n'_1} \delta_{n_2 n'_2} \delta_{n_3 n'_3} + \delta_{n_1 n_3} \delta_{n_2 n'_2} \delta_{n'_1 n'_3} + \delta_{n_1 n'_1} \delta_{n_2 n'_2} \delta_{n'_1 n_3}) \quad (52)$$

$$+ (\mathbb{E}[W^2] \mathbb{E}[W^4] - 3\mathbb{E}[W^2]^3) \delta_{n_2 n'_2} \delta_{n_1, n'_1} \delta_{n_1, n_3} \delta_{n_1, n'_3} \quad (53)$$

Details of constructing the ACE basis

Rank test

Numerical Rank The design matrix considered was constructed by evaluating all basis functions on all sites in the unit cell and summing up their values. This way we obtained a matrix Ψ of the size ($\#$ basis \times $\#$ configurations). The rank of Ψ was computed by counting the number of non-zero singular values of the matrix with a tolerance of $n * \epsilon$, where n is the smallest dimension of the matrix and ϵ is the machine epsilon of the type `Float64` in the Julia programming language ($2.220446049250313e - 16$).

Details of the standard ACE basis For the ACE basis we used a cutoff radius of 10. The maximum degree of each body-order was increased gradually until the numerical rank stopped increasing. The other parameters of the basis are identical to the one used in [38] as implemented in `ACE.jl`

Details of the Tensor-reduced ACE basis For the Tensor-reduced ACE basis we also used a cutoff of 10 Å. At each of the body order we used a maximum radial polynomial degree of 21, meaning that the radial functions were a random combination of the 21 radial polynomials. For the angular part we used maximum L of the spherical harmonics for each of the correlation orders as follows: 1 \Rightarrow 0, 2 \Rightarrow 12, 3 \Rightarrow 10, 4 \Rightarrow 8, 5 \Rightarrow 6. The motivation for having lower L for higher correlation order stems from the expectation that higher body order contribution will be smoother.

Linear ACE models

The models had a cutoff of 4.5 Å. The models were fitted using linear least squares regression with Laplacian preconditioning regularization as detailed in Ref [38]. The basis size was increased by gradually increasing the maximum polynomial degree of the ACE basis, with the inclusion of up to 4-body basis functions. The Tensor-reduced ACE basis also included up to 4-body features and was grown by increasing the number of embedding channels.

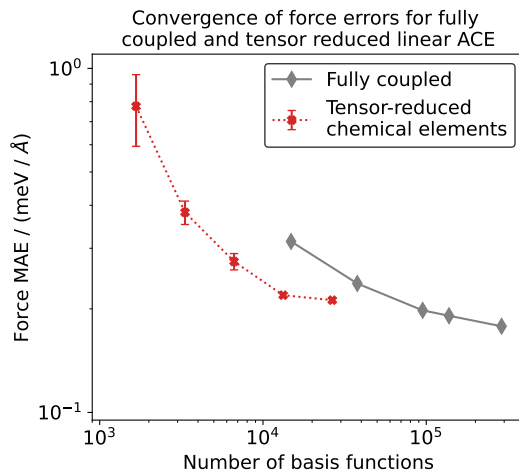


FIG. 5. Convergence of linear Tensor-reduced ACE force error to the fully coupled with increasing number of channels. Error bars show the standard error in the mean, computed across 5 fits using independently chosen random weights

Information Imbalance

The SOAP descriptors were computed using a radial cut-off of 5 \AA , $n_{\max} = 8$, $l_{\max} = 4$, $\sigma_{\text{at}} = 0.5 \text{ \AA}$ and the weight of the central atom set to 0. Shorter versions of the full power spectrum were computed using $n_{\max} = 2l_{\max}$ for $l_{\max} = 1, 2, 3$.

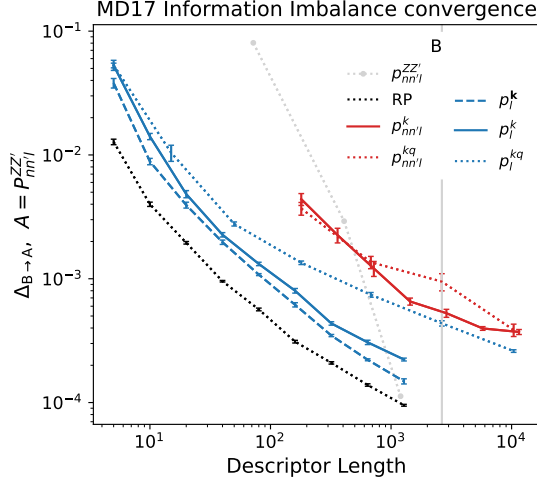


FIG. 6. Convergence of the information imbalance with respect to descriptor length for 2000 carbon environments randomly selected from the revised MD17 dataset [43]. Element and element-radial mixing are indicated using red and blue respectively. Fully coupled channels are indicated with a dotted line whilst uncoupled channels are indicated with a solid (or dashed) line. The black dotted line is RP on the full power spectrum. Error bars show the standard error in the mean computed across 10 (20 for the red lines) randomly chosen sets of weights. The grey line corresponds to using the full power spectrum truncated using $n_{\max} = 2l_{\max}$ for $l_{\max} = 1, 2, 3$ where $l_{\max} = 4$ is the reference used for all comparisons.

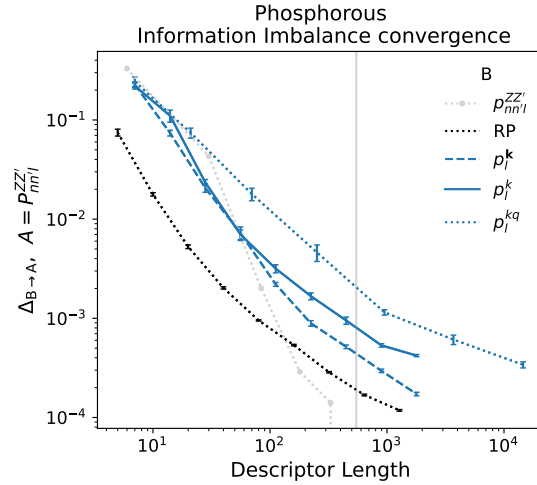


FIG. 7. Convergence of the information imbalance, relative to the full SOAP power spectrum, is shown as a function of descriptor length for a dataset of P environments. The dataset was constructed by extracting 2000 environments from the training dataset of ref. [44] using CUR decomposition and the same SOAP parameters as the original work [42] were used. Fully coupled channels are indicated with a dotted line whilst uncoupled channels are indicated with a solid (or dashed) line. The black dotted line corresponds to a random projection of the full power spectrum. Error bars show the standard error in the mean computed across 10 randomly chosen sets of weights. The grey line corresponds to using the full power spectrum truncated using $n_{\max} = 2l_{\max}$ for $l_{\max} = 1, 2, 3, 4, 5$ where $l_{\max} = 6$ is the reference used for all comparisons.

SOAP-GAP energy convergence

The `gap_fit` command used to fit one of the models is shown below. The same parameters were used for all models with only the `compress_file` being changed. Note that for brevity only one example for each descriptor type has been included. For the actual models a two-body term was included for every pair of elements and a SOAP term was included for every element.

```
at_file=db_HEA_reduced.xyz core_param_file=pairpot.xml core_ip_args={IP Glue} sparse_jitter=1e-8
gp_file=ER_diag_normal_K=64_2.xml rnd_seed=999 default_sigma={ 0.002 0.1 0.5 0.0}
gap={ {distance_2b cutoff=5.0 cutoff_transition_width=1.0 covariance_type=ard_se delta=10.0
theta_uniform=1.0 n_sparse=20 Z1=42 Z2=42 add_species=F} :
{soap_turbo species_Z={23 41 42 73 74} l_max=4 n_species=5 rcut_hard=5 rcut_soft=4 basis=poly3gauss
scaling_mode=polynomial radial_enhancement=0 covariance_type=dot_product add_species=F delta=1.0
n_sparse=2000 sparse_method=cur_points zeta=6 compress_file=ER_diag_KK_normal-8-4-5-64_2.dat
central_index=1 alpha_max={8 8 8 8 8} atom_sigma_r={0.5 0.5 0.5 0.5 0.5}
atom_sigma_t={0.5 0.5 0.5 0.5 0.5} atom_sigma_r_scaling={0.0 0.0 0.0 0.0 0.0}
atom_sigma_t_scaling={0.0 0.0 0.0 0.0 0.0} amplitude_scaling={0.0 0.0 0.0 0.0 0.0}
central_weight={1.0 1.0 1.0 1.0 1.0}}
```

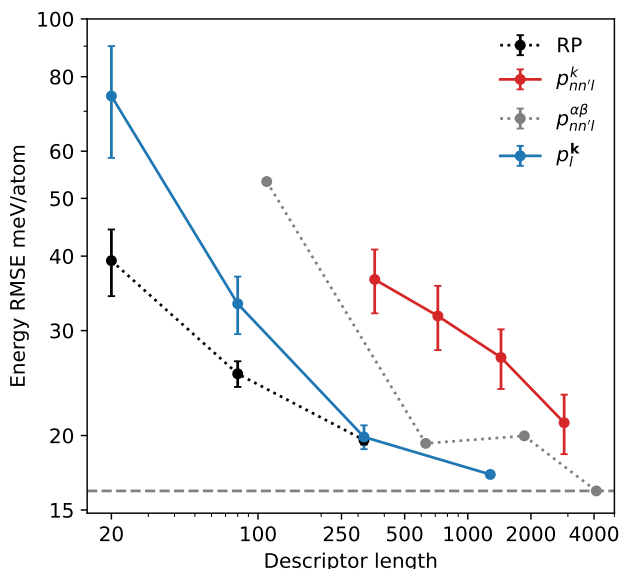


FIG. 8. Convergence of energy errors on the test set as a function of descriptor length for various GAP models. The grey line is full SOAP using $n_{\max} = 2l_{\max}$, for $l_{\max} = 1, 2, 3, 4$. The black dotted line is RP on the full power spectrum whilst the red and blue lines use a tensor-reduced features with element and element-radial mixing respectively. Error bars show the standard error in the mean, computed across 5 fits using independently chosen random weights.

Details of the MACE models

The MACE models were trained on NVIDIA A100 GPU in single GPU training. The training, validation and test split of the HME21 dataset [48, 49] were used. The data set was reshuffled after each epoch. We constructed three separate models, two with one layer and one with two layers. On all models, we used 256 uncoupled feature channels, $l_{\max} = 3$ and pass invariant messages $L_{\max} = 0$ only. For the model with random weights, we froze the weights of the initial chemical embedding. For all models, radial features are generated using 8 Bessel basis functions and a polynomial envelope for the cutoff with $p = 5$. The radial features are fed to an MLP of size [64, 64, 64, 1024], using SiLU nonlinearities on the outputs of the hidden layers. The readout function of the first layer is implemented as a simple linear transformation. For the model with the second layer, the readout function of the second layer is a single-layer MLP with 16 hidden dimensions. We used a cutoff of 6 Å. The standard weighted energy forces loss was used, with a weight of 1 on energies and a weight of 10 on forces [22].

Models were trained with AMSGrad variant of Adam, with default parameters of $\beta_1 = 0.9$, $\beta_2 = 0.999$, and $\epsilon = 10^{-8}$. We used a learning rate of 0.01 and a batch size of 5. The learning rate was reduced using an on-plateau scheduler based on the validation loss with a patience of 50 and a decay factor of 0.8.